Computational optimisation of optical projection tomography for 3D image analysis

Tang, X.

Chapter 3

Deblurring Images from 3D Optical Projection Tomography Using Point Spread Function Modelling

This chapter is based on the following publications:

Tang X., Lamers G.E.M. & Verbeek F.J. (2018), 3D Image Quality Improvement for Optical Projection Tomography via Point Spread Function Modelling. *In Imaging and Applied Optics 2018 (3D, AO, AIO, COSI, DH, IS, LACSEA, LS&C, MATH, pcAOP), OSA Technical Digest (Optical Society of America, 2018)*, paper 3W5G.5.

Tang, X., Lamers, G. and Verbeek, F. (2019). 3D Image Deblur using Point Spread Function Modelling for Optical Projection Tomography. *In Proceedings of the 12th International Joint Conference on Biomedical Engineering Systems and Technologies - Volume 2: BIOIMAGING*, ISBN 978-989-758-353-7, pages 67-75. DOI: 10.5220/0007237700670075.

Chapter summary

Optical projection tomography is successfully used in the life-sciences for 3D imaging of specimens of size between 1 mm and 10 mm. However, this requires imaging of large specimens at a large depth of field, which normally results in blur in imaging process, i.e. it compromises the image quality or resolution. Yet, it is important to obtain the best possible quality 3D image from the OPT, therefore deblurring of the image is important. The imaging process is modelled through the point spread function: the imaging of a point light source through the lens system. In this chapter we first model the point spread function along optical axis which varies at different depths in the OPT imaging system. Subsequently, the magnification is taken into account in the point spread function modelling. Deconvolution in the coronal plane based on the modelled point spread function is implemented to correct for blurring. Experiments with the proposed approach based on 25 3D images including 4 different categories of samples, indicate the effectiveness of quality improvement assessed by image blur measures from both the spatial and frequency domain.

3.1 Introduction

Here we introduce the origin for imaging blur in optical projection tomography (OPT) and elaborate our motivation of deblurring the 3D image using the point spread function (PSF). The aim of our contribution is to improve the visual resolution by deblurring the 3D OPT image by means of deconvolution based on the modeled PSF of the imaging system. This will, for large samples with a focal plane being at or away from the centre of rotation (CoR), recuperate the imperfections of 3D image resulting from the imaging system. The method for the PSF modelling will be explained in Section 3.2 and the qualitative and quantitative image comparison will be presented in Section 3.3. In Section 3.4 we will give our conclusions.

3.1.1 Background: 3D image deconvolution

As mentioned in Chapter 1 (cf. § 1.1), OPT is an optical 3D imaging technique typically for objects at tissue-, organ- and organism-level in the magnitude range of millimeters, thereby filling a gap between confocal and computational tomography imaging in the resolution range. We use depth of field (DoF) to assess the image quality - DoF is defined as the distance between the nearest and the furthest objects in an image that are in acceptable sharp focus. A point object located within the DoF of the optical system is considered to be in focus, but not necessarily in optimal focus. Beyond the DoF, the object is out of focus [32]. DoF in OPT imaging system is shaped as a double fan symmetric around the focal plane. For OPT imaging and reconstruction, the DoF is expected to be large enough to contain as much of the sample as possible. In this manner the parts of the sample located in the DoF will result in an image more or less in focus. However according to previous studies [32],[33], a large DoF subsequently introduces image blur resulting in low in-focus image quality. The image quality in this chapter is also referred to as image resolution according to some literatures [53], i.e. the extent to which detail can be observed. The trade-off between DoF and image quality should be considered when selecting lens for an OPT imaging system. A lens with low numerical aperture (NA) will produce a large DoF, allowing imaging of larger samples but results in a relatively blurred image.

A 3D image is reconstructed from the OPT tomogram that are obtained by rotating the specimen and acquiring a series of wide-field images at regular angular intervals. This is accomplished over a full revolution of the specimen. The Filtered Back Projection (FBP) algorithm is typically used for 3D image reconstruction [54] in this case, cf. § 2.2. Deconvolution applied to the reconstructed 3D image is defined as 3D image deconvolution in this thesis.

A typical way to improve the image quality to meet the resolution in the best possible way is the application of deconvolution on each reconstructed slice at individual depth, using a constant theoretical or experimental PSF. This is commonly used in 3D scanning microscopy, e.g. confocal laser scanning microscopy (CLSM), where the images

acquired from microscopy are actually a subset of reconstruction slices. However, this approach, in terms of constant PSF deconvolution, is not strictly suitable for OPT imaging. Because the imaging PSF within the DoF in OPT system, varies at different depths along the optical axis. It is, therefore, necessary to model this variation in OPT imaging, which can be subsequently used for 3D image deconvolution. This explains our motivation for PSF modelling in OPT imaging system.

According to Chen *et al.* [55], OPT is typically performed with specimens that extend beyond the Rayleigh length or Rayleigh range of the imaging lens. Therefore, the tangential resolution of the reconstructed 3D image decreases away from the focal plane in a radial manner. When the focal plane coincides with CoR, the tangential resolution, centred at the CoR, decreases in a radial-symmetrical fashion. For an imaging system with a focal plane located away from the CoR the decrease in resolution is more complicated but the highest resolution is still found around the focal plane. In this case the focal plane in the reconstructed slice corresponds to a circle centred at the CoR, rather than a point coincident with the CoR. This subsequently appears as a cylindrical surface in the 3D image centred at the CoR.

The tangential resolution of the OPT 3D image slice decreases radially around the focal plane. Theoretically, the best resolution of the reconstructed 3D image can be achieved by combining all the coronal deconvolutions of different sample angles. The coronal deconvolution means deconvolving the 3D image with the PSF slice by slice in the coronal plane along its depth axis. This depth axis is parallel to optical axis of the modelled PSF. We will only implement the coronal deconvolution in 2 opposite angles, i.e. the reconstructed 3D image and its opposite sample at 180° centred at the CoR, in parallel considering the enormous time consumption of 3D matrix rotation in N angles and the symmetry of the focal plane. When the focal plane is off the CoR during the imaging process, the shift is accounted for by a shift in the model of the PSF.

In this chapter we focus on the presentation of the concept of PSF modelling and coronal deconvolution on 3D OPT data, accompanied by some initial experimental results based on 25 3D images including 4 different categories of samples. Further evaluations on a larger number of data are point of our current research.

3.1.2 Related work

Accounting for the trade-off between large DoF and high resolution, previous studies have proposed several methods to this problem. One possibility is choosing a high NA lens to acquire a high-resolution image and combining multiple focal planes in a simultaneous manner [56] or scanning the focal plane through the sample [57] (Miao *et al*., 2010) . These multiple focal plane approaches solve the issue of narrow DoF, but the mechanism of multiple measurements and scanning increases the acquisition time and the complexity of the imaging system. Another direction is to use a reasonable NA lens and deblur the image by employing a deconvolution or filter on images before or after reconstruction. Walls *et al.* [32] first applied the frequency-distance relationship (FDR) [58]

in OPT. The corresponding filter was implemented on the sinogram prior to reconstruction. The quality of the 3D image can be further improved with weighted filtered back projection (WFBP) [59]; this is accomplished by considering the intensity distribution of multiple fluorescent spheres of known size along the optical axis. But the implementation of evenly placing each sphere along the optical axis is rather difficult to achieve. Chen *et al.* [55] proposed a way to determine the modulation transfer function (MTF) that contributed to MTF-mask filter and MTF-deconvolution filter in the reconstruction process. The former filter significantly reduced the artifacts produced by sparse projection but the latter filter had limited improvement on tangential image resolution. Additionally, a spatial-invariant experimental PSF was investigated by McErlean *et al.* [60] in order to improve the spatial resolution. However, spatial-invariance of the PSF is not entirely convincing for OPT. Most recently, a new deconvolution approach based on the reconstructed 3D image was proposed by Horst *et al.* [53]. In their approach the PSF was modelled and as such they achieved significant improvement on the reconstructed slice. Nevertheless, they focused on the deconvolution of vertically independent slices and omitted the PSF diffractions along the optical axis that concerns the interaction of different slices.

In this chapter, we present our contribution by modelling an experimental PSF from a single sphere along optical axis, thereby considering the interaction of contiguous slices from the reconstructed volume. At the same time, the magnification, as obtained from a zoom lens, is taken into account in the experiments.

3.2 Materials and methods

In order to model the PSF for our OPT imaging system, we first propose a protocol to prepare for the imaging of a point source, i.e. a fluorescence sphere or bead. The modelling approach will then be introduced and elaborated. This approach will be subsequently used for the deconvolution of 3D image in OPT.

3.2.1 Sample preparation of a single fluorescence sphere

To image the specimens in the range of several millimeters small-valued NA lens is used to obtain the large DoF in our OPT imaging system, i.e. effective NA: 0.0105~0.0705 as part of a Leica Stereo Microscope. The resolution of an optical system is defined as the minimum distance r at which two separate points can be distinguished as individuals. According to the Rayleigh criterion $r = 0.61 * \lambda/NA$ for a circular aperture with $\lambda = 509\ nm$ is the emission wavelength, the minimum size of the experimental fluorescence sphere is supposed to be in the range between 4.40 μ and 29.57 μ. To make it visible in the image the sphere size is supposed to exceed this range. In our case, we choose the fluorescence sphere of size 43.2 μm and diluted it to a concentration of 360 $beads/ml$.

Figure 3.1. The injection protocol with green spots indicating the injection position of fluorescence spheres. The cylinder corresponds to the shape of the agarose block as mounted in the OPT.

To image and model the PSF along optical axis we have developed an injection-based protocol to place the spheres into agarose as follows:

- 1% low melting point (LMP) agarose, cool down to ~37°;
- Drill cylindrical agarose shapes when it is semi-solidified in a petri dish;
- Inject the diluted spheres into the outer wall of the agarose along a line parallel to the central axis, preferably with a small size syringe. We use a 0.5 ml syringe with a needle length of $13\ mm$ and diameter of $0.29\ mm$, as shown in Figure 3.1;
- Keep the agarose at 4℃ until it is fully solidified (~3 hours);
- Clear the sample with 70%, 80%, 90%, 96%, 100% ethanol, 100% ethanol: BABB (benzyl alcohol: benzyl benzoate = 2: 1) = 1: 1 and BABA.

Our goal is to acquire the images of a single sphere placed at different depths along optical axis. Therefore, randomly sprinkling the spheres into the agarose in a traditional way is not feasible. The main reason is that there may be interactions and overlap between different spheres either at the same or different depths. This makes the selection for imaging of a single sphere image difficult or even impossible. The images of each single sphere at different depths are acquired by means of sample rotation. Each rotation corresponds to a different depth in the OPT imaging system. The sphere injection method in of our protocol significantly reduces the probability of overlapping between different spheres. In this way the images of the same sphere in a full revolution can be easily and efficiently acquired. The OPT imaging system and environment is configured as explained in chapter 1 cf. § 1.2.

3.2.2 PSF modelling concerning different magnifications

For our experiments the acquisition of a single sphere comprises a full revolution in 0.9° steps resulting in 400 images. In Figure 3.2 the processes of sphere image acquisition and PSF modelling are depicted. In Figure 3.2(a) and (b), the green dot represents the sphere and the red arrow indicates the sphere rotation. The excitation and emission beams are regarded to be parallel. This is indicated by blue and green arrows in Figure 3.2(a). For

PSF modelling, the focal plane is set at the CoR. The 3D image whose focal plane is shifted from the CoR, requires an equal shift in the PSF. With the protocol (cf. section 3.2.1) the physical rotation radius of the sphere r_b can be easily measured. To this end, we first measure the radius of the cylindrical agarose r_c and image it in the bright-field mode with short exposure time. In the same experimental environment, the sphere is afterwards imaged in the fluorescence mode. r_b is calculated as:

$$r_b = \frac{d_{bi}}{d_{ci}} \cdot r_c \tag{1}$$

with d_{bi} representing the rotation diameter of the sphere in the tomogram, achieved by measuring the distance of two opposite sphere centres that are both in focal plane. d_{ci} is the diameter of the cylindrical agarose in the bright-field image. Dividing r_b by the number of steps required for a rotation of $\pi/2$, i.e. the rotation radius r_b, the depth of each rotation step along optical axis is approximately determined as $r_b/100$ [*]. In our case the measured $r_c = 4\,mm$, $d_{bi}/d_{ci} = 0.751$, producing $r_b \approx 3\,mm$. Therefore, the physical distance of two adjacent rotations along optical axis is approximately 30 μm.

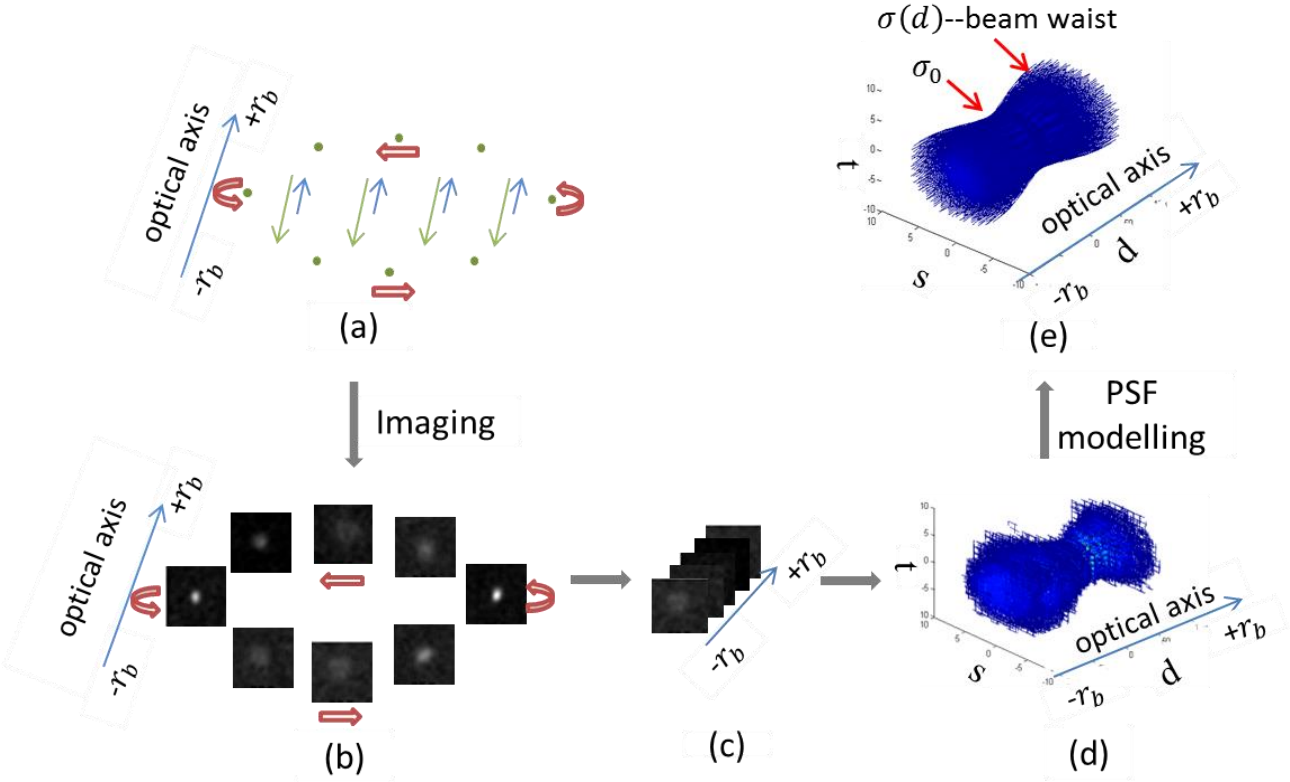

Figure 3.2. Image acquisition and PSF modelling of a single fluorescence sphere. (a) The light path of the OPT imaging system that passes through fluorescence sphere (green dot). The excitation beams and emission beams are separately shown as blue and green arrows. (b) Images of the single sphere acquired at different angles. (c) Images of the single sphere stacked according to the defocus. Half rotation with defocus range $[-r_b, +r_b]$ is required, in our experiment $r_b = 3\,mm$ as calculated from Eq. (1). (d) The experimental and discrete PSF with defocus $[-r_b, +r_b]$. (e) The modelled and continuous PSF with defocus $[-r_b, +r_b]$.

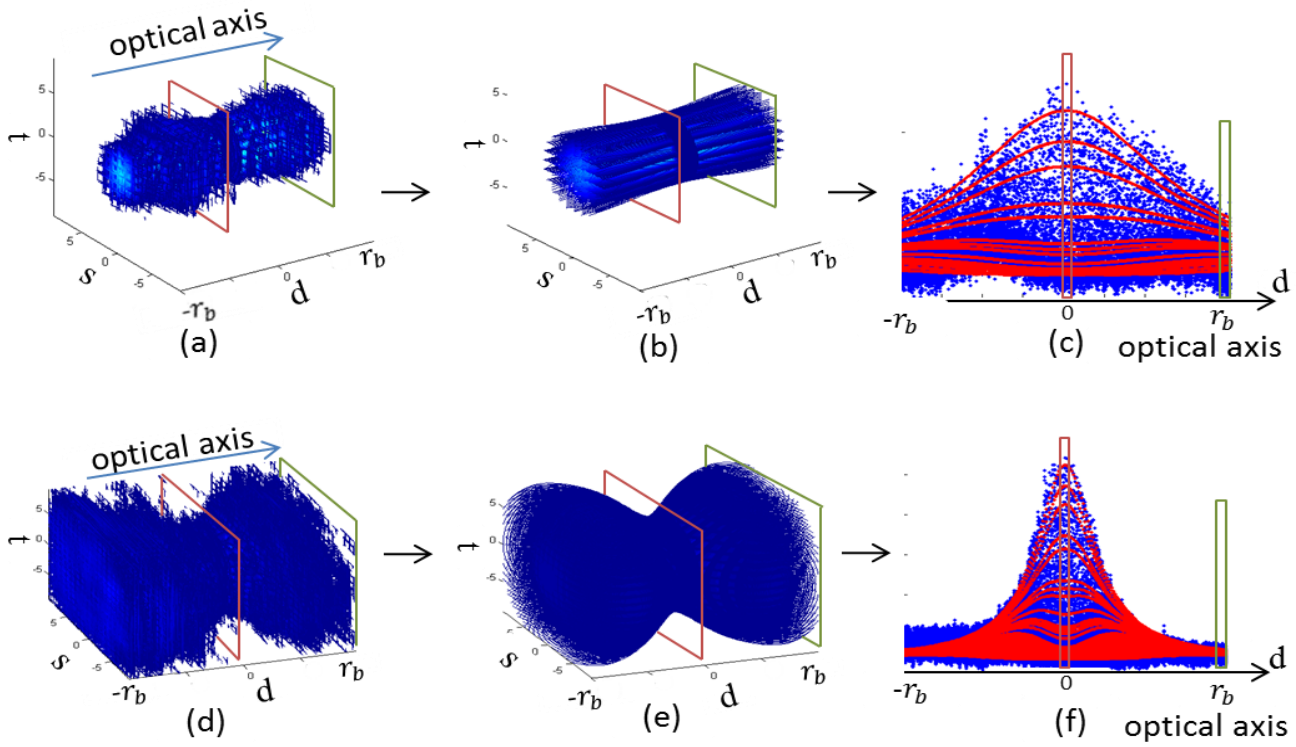

Figure 3.3. PSF modelling along the optical axis. (a), (d) Experimental PSFs acquired from images at magnification of 12.5 × and 25.0 ×. (b), (e) The corresponding modelled PSFs using Eq. (4) and Eq. (5). All the voxels of experimental data in (a) and modelled data in (b) are respectively transformed to blue and red dots in 1D functional in (c) to visualize the modelling performance. The vertical axis in (c) displays the intensity that corresponds to the voxel intensity in (a) and (b). Similarly, voxels in (d) and (e) are transformed to the data in (f).

According to the definition, the optical imaging PSF is assumed as a focused Gaussian-like beam [61], i.e:

$$p(s,t,d) = \frac{1}{2\pi\sigma(d)^2} \cdot exp(-\frac{s^2+t^2}{2\sigma(d)^2}) \quad (2)$$

Where s, t, d are the three axes in 3D space, with d being the optical axis. The $\sigma(d)$ is beam waist (Figure 3.2) given by:

$$\sigma(d) = \sqrt{\sigma_0^2 + (\frac{\lambda d}{\pi\sigma_0})^2} \quad (3)$$

with σ_0 the Gaussian beam waist defined as the $1/e$ value of the field amplitude in focus, λ the emission wave length of fluorescence spheres and d the defocus along optical axis.

For a specific magnification, σ_0 is constant, but it varies when imaging with different magnifications. Additionally, in Eq. (2) and Eq. (3) the beam waist $\sigma(d)$ is typically regarded as the standard deviation of the Gaussian model in previous studies [53]. Different from the Gaussian model [53], we can further generalize the model by employing parameters ρ_1, ρ_2 and ρ_3 as follows:

$$p(s,t,d) = \rho_1 \cdot \frac{1}{2\pi\sigma(d)^2} \cdot \exp(-\frac{s^2+t^2}{2\sigma(d)^2})^{\rho_2} + \rho_3 \quad (4)$$

Instead of equalizing the beam waist and standard deviation as described in [53] and [61], we investigate the relationship between them by multiplying a parameter a with beam waist, thereby considering different magnifications; thus,

$$\sigma(d) = a \cdot \sqrt{\sigma_0^2 + (\frac{\lambda d}{\pi\sigma_0})^2} \quad (5)$$

To relate the beam waist in focus σ_0 and the scale parameter a to the magnification, 6 magnifications i.e. 12.5 ×, 15.0 ×, 17.5 ×, 20.0 ×, 22.5 ×, 25.0 ×, are configured to acquire the images of the same sphere. The magnifications are obtained through zooming. The magnification of 12.5 × approximately corresponds to the minimum magnification that renders the sphere visible in our experiment, while 25.0 × approximates to the maximum magnification that confirms that a full revolution of the sphere remains in the field of view (FoV). The PSF of each magnification is modelled by creating an optimisation problem and solving it with least square curve fitting. The overall fitting error of the 6 experimental PSFs is 5.00%. The experimental PSFs acquired from images with magnification of 12.5 × and 25.0 × are shown in Figure 3.3 (a) and (d) respectively. The color of the voxel indicates the intensity of PSF response. (b) and (e) represent the modelled PSFs of the two magnifications. Voxels in 3D space are converted to a 1D space with horizontal axis approximating the optical axis and vertical axis displaying the intensity. The 3D voxels on the slice in (a) and (b) match the 1D points in the box in (c) according to the same color. The experimental PSF differentiation between two magnifications is evident in (a) and (d). By transforming the 3D space to 1D functional, we can intuitively visualize and understand the distribution of the experimental PSF (blue dots) and the modelled PSF (red dots), as well as showing the differences between them.

With the proposed modelling approach on our data, the parameters ρ_1, ρ_2 and ρ_3 have proven to be constant regardless of magnification: $\rho_1 \approx 0.0041$, $\rho_2 \approx 1.0549$ and $\rho_3 \approx 2.9 \times 10^{-5}$. The beam waist σ_0 and parameter a related to the magnification range are estimated as depicted in Figure 3.4. We imply to the model that the fitting errors on the observed data are minimal. We, therefore, employ exponential and a quadratic function respectively. As shown in Eq. (6) and Eq. (7), x represents magnification and p_1 to p_5 are the model parameters.

$$\sigma_0 = p_1 \cdot e^{p_2 x} \quad (6)$$

$$a = p_3 x^2 + p_4 x + p_5 \quad (7)$$

The PSF of any 3D image between $-\infty$ and $+\infty$ along optical axis can be modelled as depicted in this section. The modelling is implemented with the focal plane set at the CoR. However, we acknowledge that in most circumstances of imaging acquisition the focal plane is not in line with the CoR, i.e. with a shift η. Consequently, the modelled PSF will be shifted along the optical axis by η from the focal plane to meet the imaging setup. Besides, the length of the PSF along optical axis is determined by the size of 3D image and the resolution r, because in 3D reconstruction each voxel in the 3D image

corresponds to each pixel in the 2D images. The NA is the effective value achieved from interpolation relating to the magnification. The relationship between effective NA and magnification is determined by the Leica objective lens.

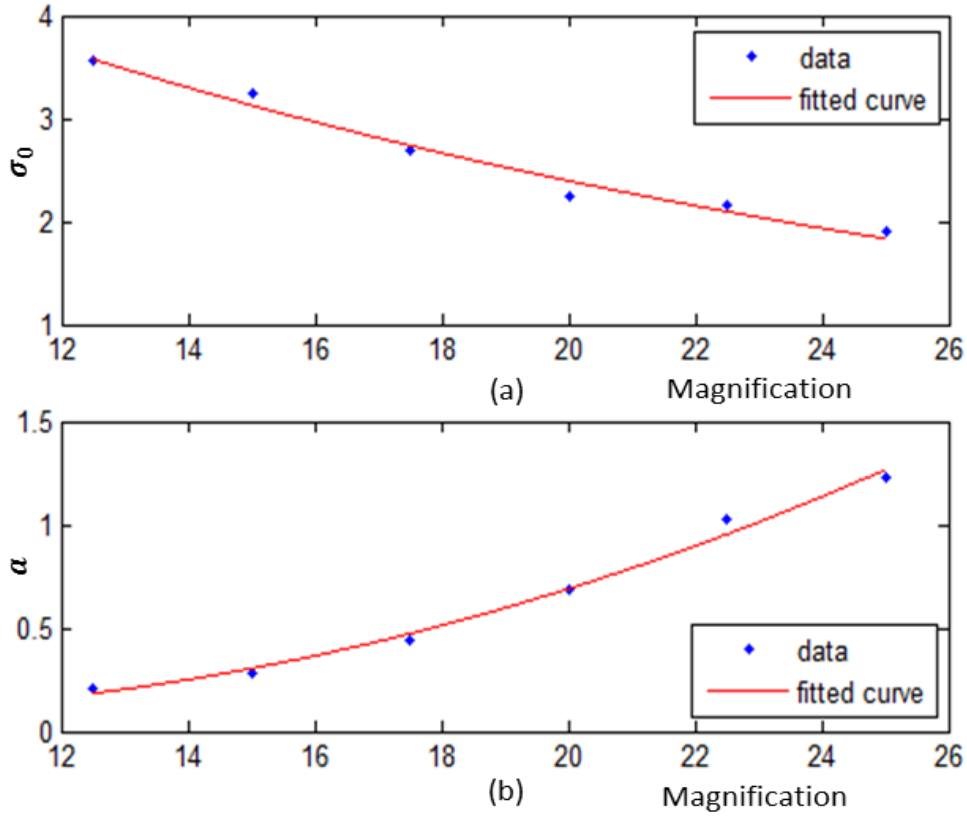

Figure 3.4. Fitting of the parameter σ_0 and a estimated from 6 magnifications. σ_0 can be fitted best by an exponential function as shown in (a) while a can be fitted best by a quadratic function in (b).

3.2.3 Deconvolution of 3D images in coronal plane

The modelled PSF consists of multiple 2D Gaussian patterns along optical axis. Therefore, the 3D image can be deconvolved slice by slice along its depth axis that is parallel to the optical axis. As the slices are coronal sections, the deconvolution is implemented on the 3D image R in the coronal plane as follows:

$$D_{(x,y,d)} = R_{(x,y,d)} *\!/\!* p_{(s,t,d)} \quad (8)$$

R is the reconstructed 3D image with the depth axis d parallel to the optical axis of the PSF. $*\!/\!*$ stands for the operation of deconvolution. Considering the shifted focal plane and the reconstruction symmetry, deconvolution of R', the opposite view of R projected along d, is executed by applying:

$$D'_{(x,y,d)} = R'_{(x,y,d)} *\!/\!* p_{(s,t,d)} \quad (9)$$

The transform from R to R' is conducted by a matrix rotation of π centred at the CoR. The 3D image with the deconvolution is then achieved by combining D and π back rotation of D'.

3.3 Experiments

The deconvolution performances of the PSF model on 3D OPT images are presented in three different ways. We first give a qualitative comparison between image slices with and without the proposed deconvolution approach. To further quantify the performance differences, we use three image blur metrics to measure the image blur and calculate the performance based on these metrics, in a slice manner. Finally, we present a holistic metric for 3D image deblurring improvement and implement it for performance comparisons. The samples used for the experiments are prepared according to our standard protocol, cf. § 1.2.4.

3.3.1 Image comparison of deconvolution

With respect to the magnifications, the experiments were conducted on images at 2 different magnifications. One is a zebra finch embryo in fluorescence mode with magnification $13.83\times$ and focal plane shifted by $-0.93\,mm$. Taking the resolution limit and the 3D image size into consideration, the calculated defocus of the PSF along the optical axis ranges from $-6.303\,mm$ to $8.063\,mm$. The deconvolution is performed using the Lucy-Richardson algorithm [62] with a same number of iterations; here 10 is used based on the balance between reconstruction quality and computational time. The result for one coronal slice is shown in Figure 3.5 (c) and for the horizontal slice in Figure 3.5 (d). The corresponding slices prior to deconvolution are displayed in Figure 3.5 (a) and (b). The comparisons of intensity profile along a line with (red) and without (blue) deconvolution are presented in (e) and (f) respectively. The comparisons of the 3D visualization results are shown in Figure 3.6.

In Figure 3.7 another sample is depicted; a specimen of zebrafish larvae. The 3D visualizations of reconstructions with and without deconvolution are displayed in Figure 3.7. Figure 3.8 compares two orthogonal image samples of the zebrafish in detail. The magnification and the shifted focal plane are separately $49.98\times$ and$-0.5\,mm$, with the computed defocus of the PSF being between $-2.242\,mm$ and $3.246\,mm$. Figure 3.8 (a) and (b) are the slices prior to deconvolution in two orthogonal planes, while (c) and (d) correspond to the deconvolution results. From visual assessment between (c) and (d), we can appreciate that the performance in the horizontal plane is almost as good as it is in coronal plane. This means that deconvolution in the coronal plane simultaneously improves the quality of the image in the horizontal plane to some extent. From a comparison of the quantitative intensity profile in the graph, we state that the proposed deconvolution sharpens and refines the 3D reconstructed images. It enhances the strong signals and makes the intensity profile more distinct.

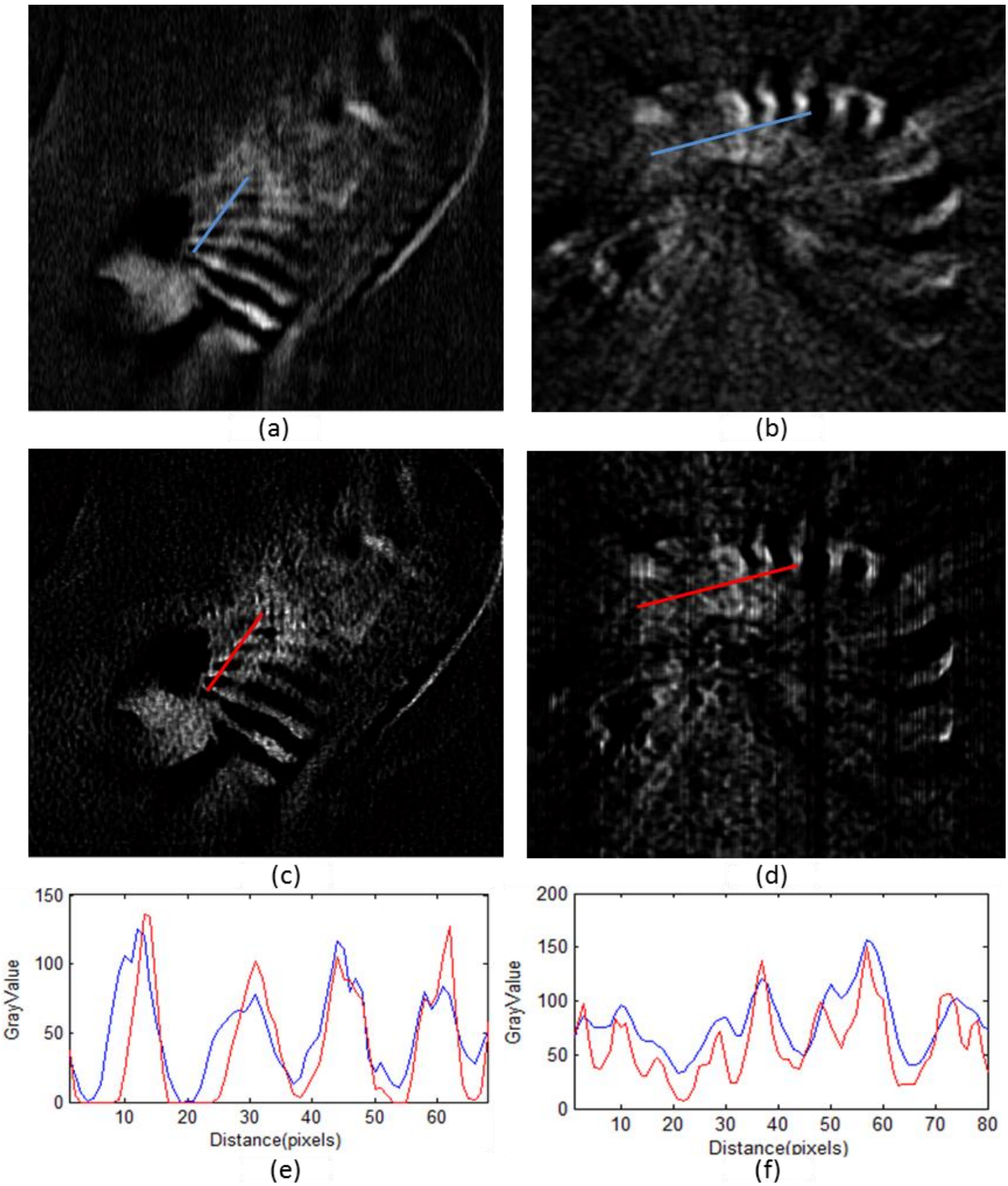

Figure 3.5. Deconvolution results. (a) The coronal slice of the 3D zebra finch with obvious blur around the ribs. (c) Distinct texture appears around the ribs after the deconvolution. (e) The comparison of intensity profiles along a line in (a) and (c). (b) and (d) The horizontal slice comparisons with the line intensity profiles shown in (f). In (c) and (d), more textures are observable in comparison with (a) and (b). In (e) and (f), the red thinner intensity profile, explains the more image sharpness along the red line in (c) and (d), comparing to (a) and (b) separately.

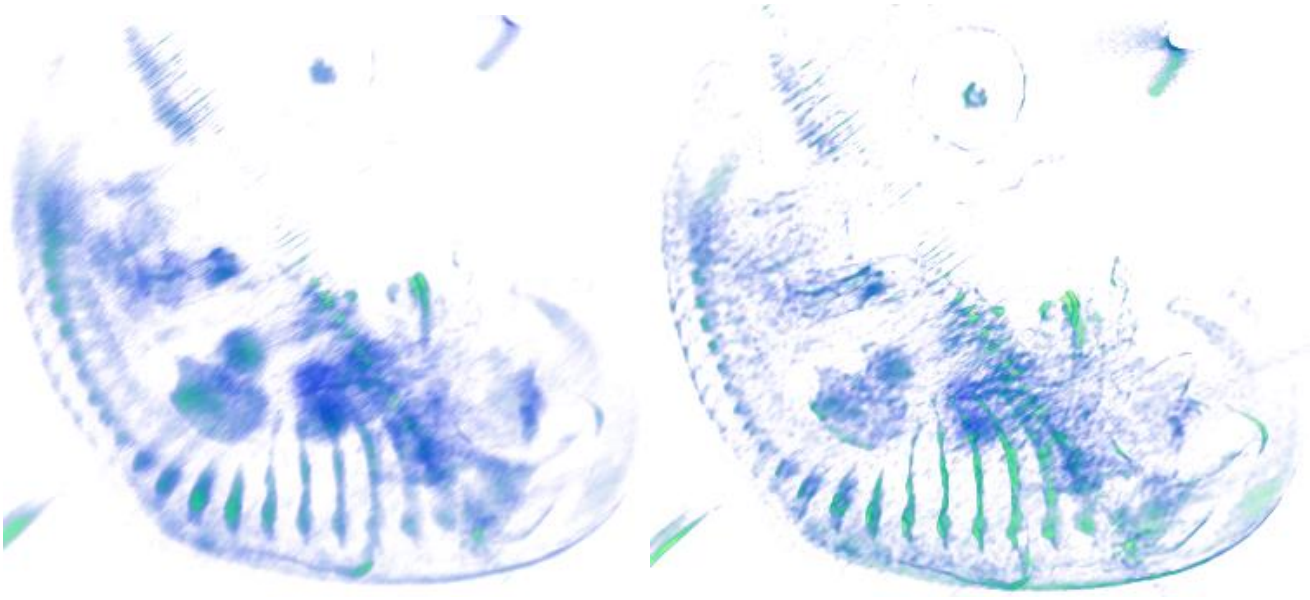

(a) **(b)**

Figure 3.6. Deconvolution results. (a) 3D visualization of the zebra finch embryo without deconvolution. (b) 3D visualization of zebra finch with deconvolution. The visualization is made with Amira software [63].

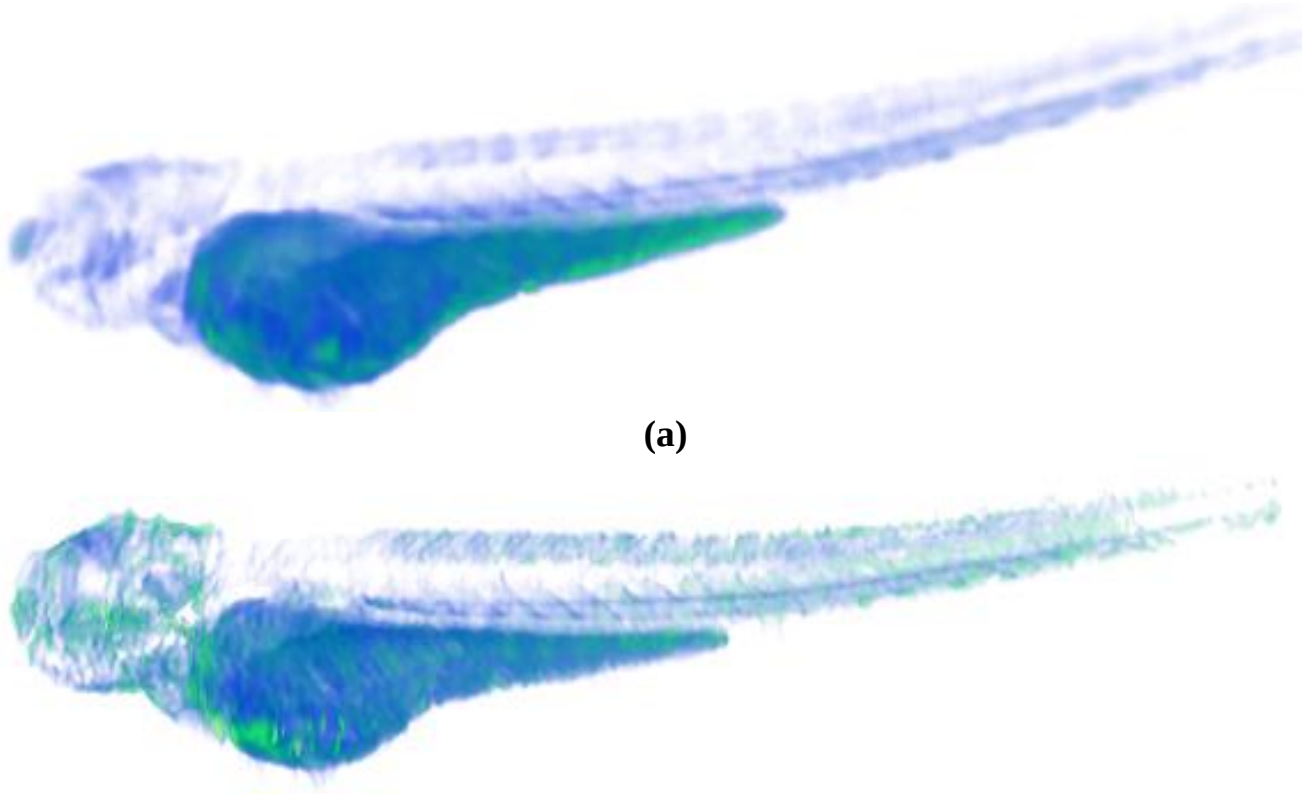

(a)

(b)

Figure 3.7. Deconvolution results. (a) 3D visualization of the zebrafish without deconvolution. (b) 3D visualization of zebrafish with deconvolution, visualized with Amira software [63].

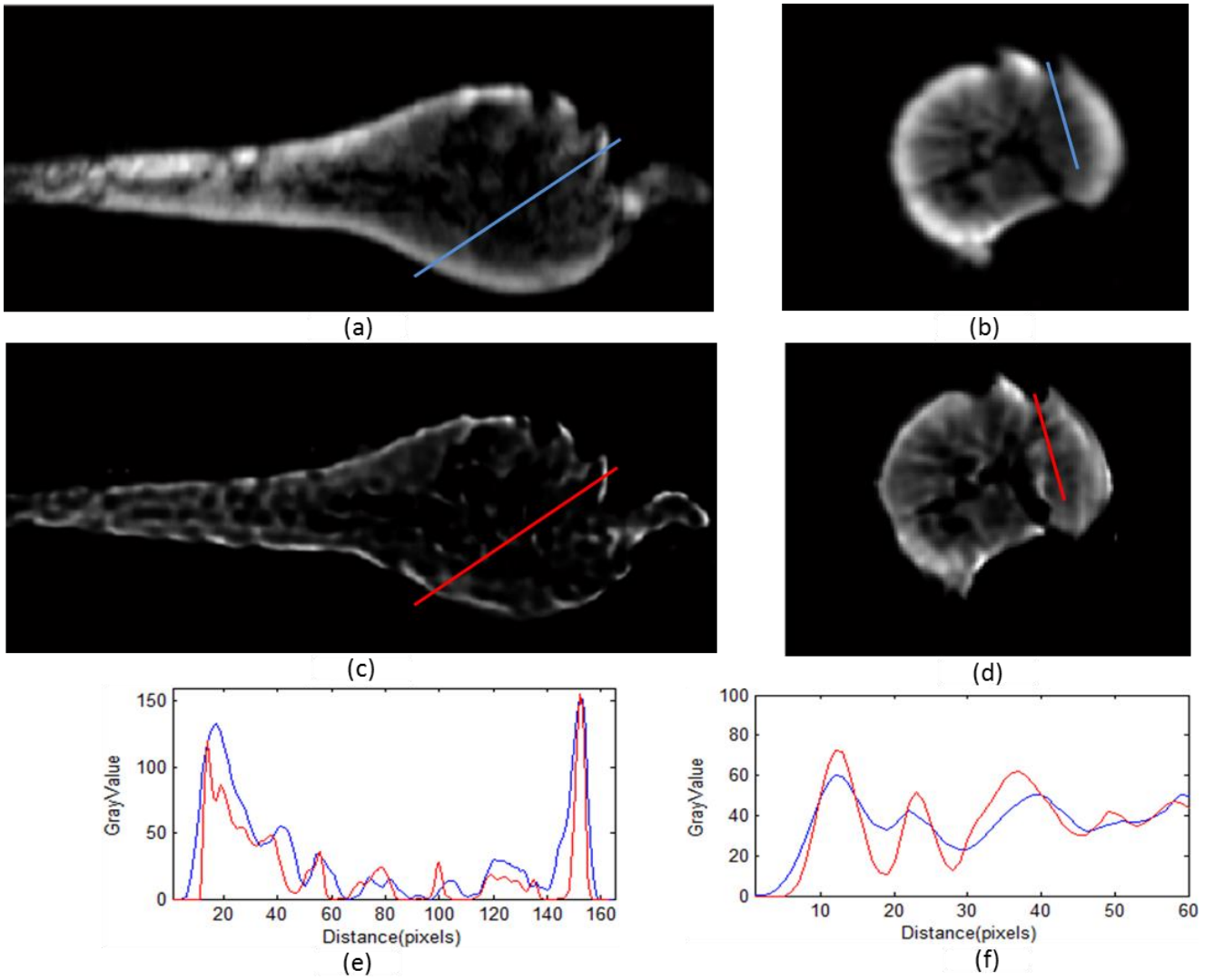

Figure 3.8. Coronal and horizontal slices of 3D zebrafish before ((a) and (b)) and after ((c) and (d)) deconvolution. The deconvolution highlights the strong signals and makes the texture more visible. (e) compares the intensity profile of the same line before (labelled as blue in (a)) and after (labelled as red in (c)) deconvolution, so does (f).

3.3.2 Image blur measurement on slices

To quantify the image blur of each slice, three metrics, known from the literature, were selected; i.e. the just noticeable blur (JNB) [64], the cumulative probability of blur detection (CPBD) [65] and the frequency measure (FM) [66]. These three metrics are employed to evaluate the performance of our method. Both the JNB and CPBD measure represent a sharpness metric by detecting and quantifying the blur in the spatial domain. Different from JNB and CPBD, the FM measure quantifies the sharpness in the frequency domain with an easier and more efficient approach. All the three metrics characterize the sharpness of an image, so the measure increases at improved image quality.

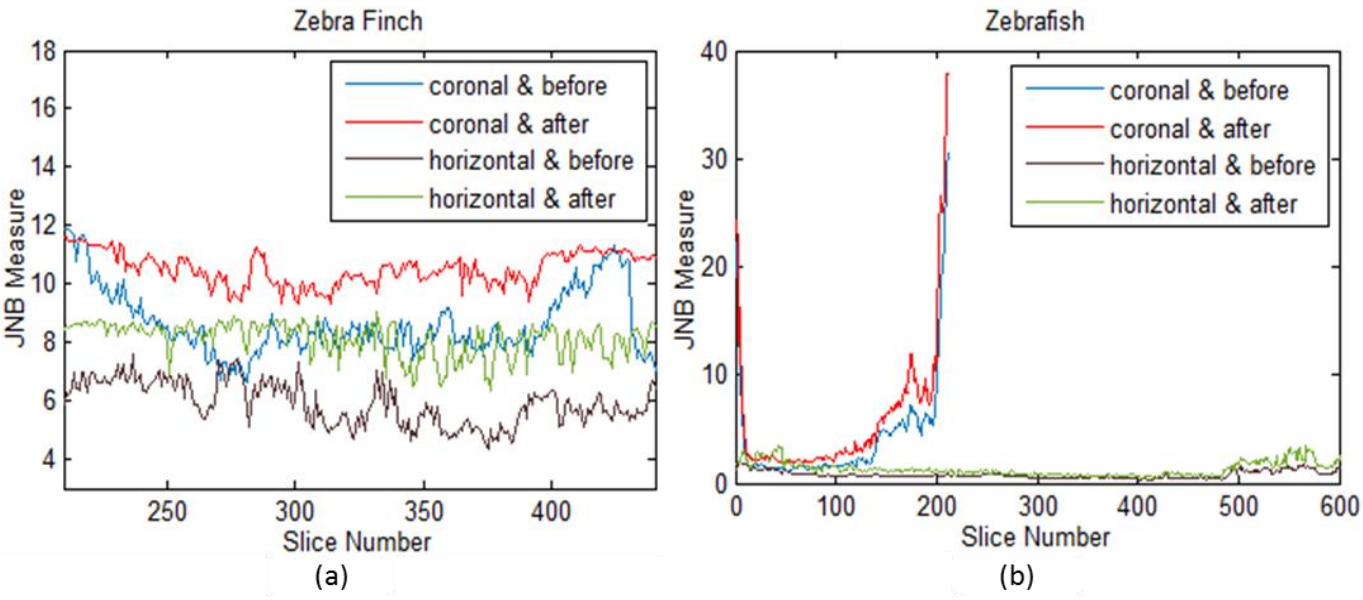

Figure 3.9. (a) JNB measure on the zebra finch data with magnification 13.83 ×. (b) JNB Measure on the zebrafish data with magnification 49.98 ×. Coronal and horizontal are the two orthogonal planes displaying the 3D image.

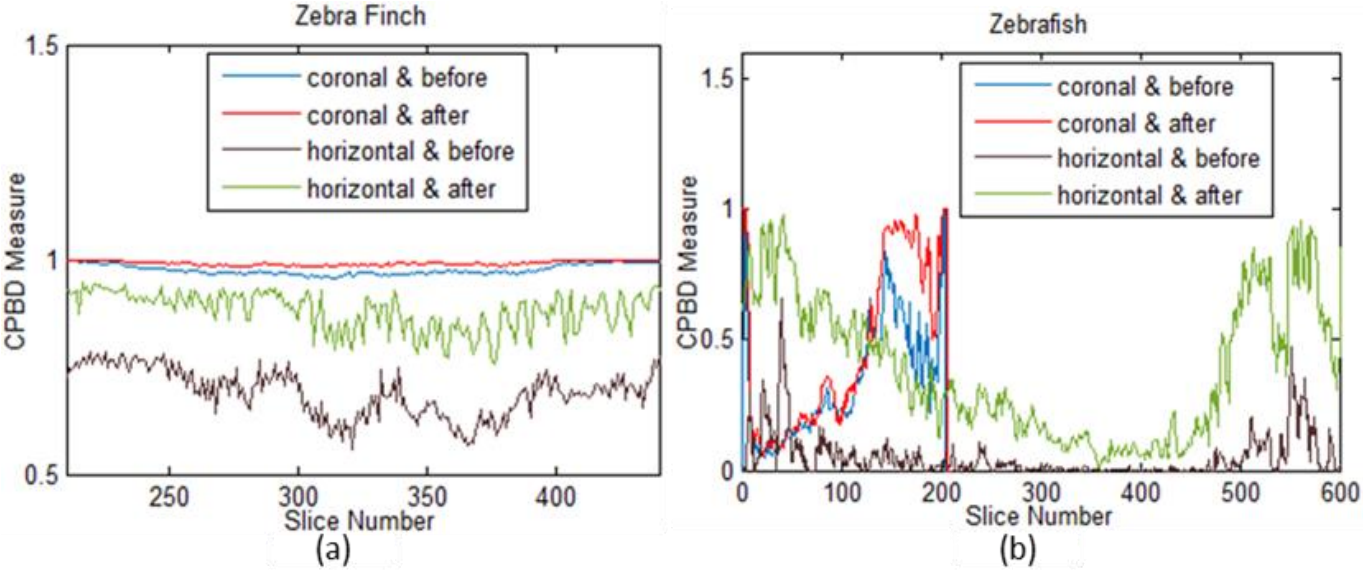

Figure 3.10. (a) CPBD measure on the zebra finch with magnification 13.83 ×. (b) CPBD Measure on the zebrafish with magnification 49.98 ×.

Whilst experiments in section 3.3.1 give us a qualitative comparison between the deconvolved slices and non-deconvolved slices, in this section we quantitatively look into all the slices in different orthogonal planes (coronal and horizontal) with the three image sharpness metrics (i.e. JNB, CPBD and FM). In the graphs depicted in Figure 3.9 - 3.11 we can observe that with all the three metrics the deconvolved slices on both planes show higher measurement values compared to the image slices without deconvolution. This means that for all the slices, regardless of orientation, the deconvolution holistically deblurs the images and thereby significantly improves the image quality.

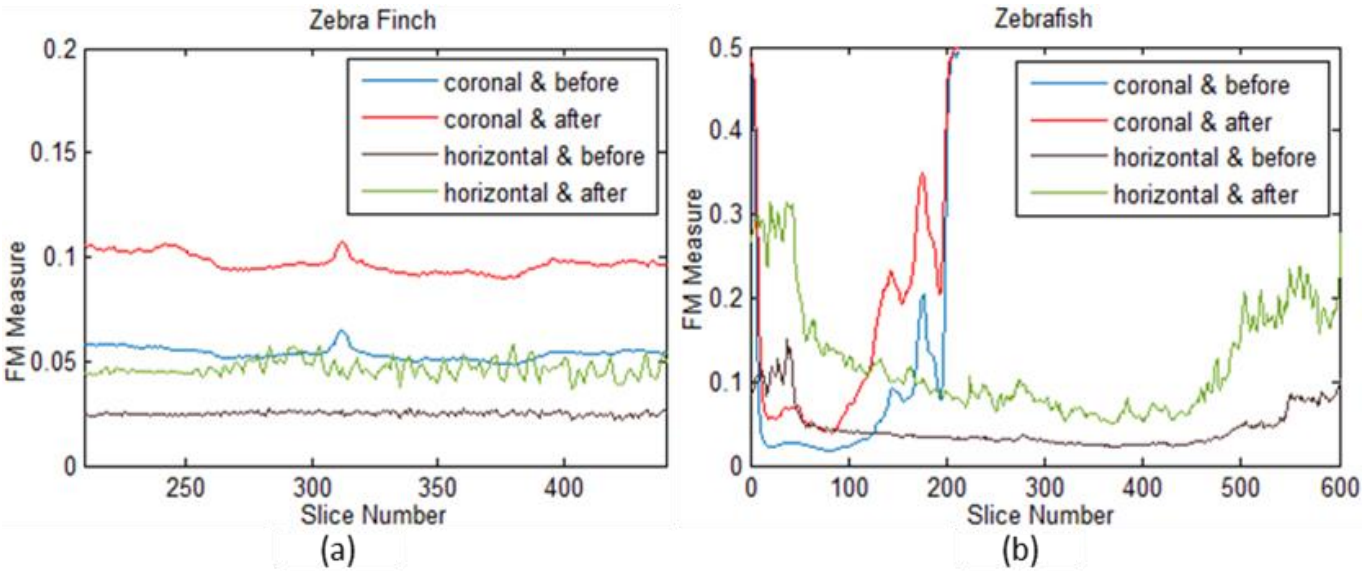

Figure 3.11. The FM before and after deconvolution on the two 3D image data. (a) FM measure on the zebra finch with magnification 13.83 ×. (b) FM Measure on the zebrafish with magnification 49.98 ×.

3.3.3 Quantitative 3D image quality improvement of deblur

To further quantify the deblur of the deconvolution results on the original reconstructed 3D data across the planes, we present the 3D image quality improvement criterion of deblur as I_{3d} in Eq. (10). Improvement in three orthogonal individuals are combined and encoded as a whole and each of them are represented as:

$$I_{3d} = \sqrt{(\frac{1}{Nx}\sum_{ix=1}^{Nx} I_{ix})^2 + (\frac{1}{Ny}\sum_{iy=1}^{Ny} I_{iy})^2 + (\frac{1}{Nz}\sum_{iz=1}^{Nz} I_{iz})^2} \quad (10)$$

$$I_{ix} = \frac{M_{ix}^d - M_{ix}^r}{M_{ix}^r}, \quad (11)$$

$$I_{iy} = \frac{M_{iy}^d - M_{iy}^r}{M_{iy}^r}, \quad (12)$$

$$I_{iz} = \frac{M_{iz}^d - M_{iz}^r}{M_{iz}^r}, \quad (13)$$

Where i is the slice number and x, y and z are the coordinate axises in 3D space. I_{ix}, I_{iy} and I_{iz} indicate the deblurring performance of slice i on the three different axises. M_{ix}^d and M_{ix}^r are respectively the ith deconvolved and original reconstructed slice on axis x. M_{iy}^d, M_{iy}^r, M_{iz}^d and M_{iz}^r are defined in a similar way on the two different axises. By employing the deblur performance I_{3d}, deconvolution performance of two different methods on the same data should be comparable.

Next, we apply our deconvolution method to 23 more 3D data sets, which contains 3 categories of samples i.e. zebrafish larvae, the adult zebrafish brain and the chicken embryo heart. They are in different stages of development and are acquired at different magnifications. It is important to realize that the metrics in this chapter cannot assess the

image blur across different data, but using the same data they are able to evaluate the performance of different deblurring approaches. Taking advantage of this, we compare the presented deconvolution method with the most commonly used Gaussian-based blind deconvolution [67]. According to our observation of the results for blind deconvolution, the kernel size does not make a visible difference on our 3D images. Therefore, we present our results for blind deconvolution with the kernel size set as 7, taking acceptable computation time into account. From the 3 metrics, i.e. CPBD, JNB and FM, we have selected the most robust metric JNB to measure the image blur of each slice. The results of the 3 categories of samples are presented in Table 3-1 to Table 3-3. For all the 23 data, our deconvolution approach outperforms the Gaussian-based deconvolution, thereby indicating the success of the method.

Table 3.1. 3D image quality improvement of 10 zebrafish embryos based on JNB Measure.

	01	02	03	04	05	06	07	08	09	10
$\mathcal{G}$	0.16	0.21	0.15	0.21	0.29	0.24	0.22	0.16	0.20	0.25
PSF_m	**1.35**	**2.10**	**1.41**	**3.23**	**1.54**	**1.50**	**1.50**	**1.37**	**1.45**	**1.70**

⋆ $\mathcal{G}$ -- Gaussian-based blind deconvolution. PSF_m -- PSF based modelling deconvolution. 10 zebrafish embryos correspond to 01-10 with age from 3 *dpf* to 7 *dpf*.

Table 3.2. 3D image quality improvement of 6 zebrafish brain based on JNB Measure.

	01	02	03	04	05	06
$\mathcal{G}$	0.25	0.29	0.26	0.24	0.01	0.21
PSF_m	**0.41**	**0.49**	**2.55**	**0.17**	**1.15**	**1.20**

⋆ 6 adult zebrafish brains correspond to 01-06 with different magnifications.

Table 3.3. 3D image quality improvement of 7 chicken heart based on JNB Measure.

	01	02	03	04	05	06	07
$\mathcal{G}$	0.24	0.16	0.19	0.26	0.27	0.18	0.32
PSF_m	**0.93**	**0.49**	**0.29**	**1.15**	**0.49**	**0.38**	**1.07**

⋆ 7 chicken embryo hearts at different stages correspond to 01-07.

3.4 Conclusions

In this chapter we have focused on 3D image deblur and quality improvement, under the condition of the limitation of small NA for imaging of large sized samples. We investigated and modeled the PSF along the optical axis, exploring the influence of magnification on PSF. The sample of a single fluorescence sphere is prepared with the protocol in section 3.2.1. The experimental PSF is then modelled to deconvolve the 3D image in a coronal plane. A number of measures for image blur are employed to convincingly evaluate the performance of the deconvolution. They provide quantitative information about how much improvement is achieved. The overall improvement I_{3d}

gives us a criterion to compare image quality improvement regardless of different data. All the experimental results including the image comparisons and quantitative measures sustain the effectiveness of the proposed PSF modelling and deconvolution methodology.

The deconvolution results presented represent a proof of concept. The datasets used in the experiments are composed of 25 samples, i.e. 4 categories: zebrafish embryo, zebra finch embryo, adult zebrafish brain and chicken embryo heart. Regarding the evaluation of performance on a large volume of different datasets, our data are far from perfect in terms of 'large dataset'. However, it presents a clear idea that our model is not constrained by samples of one particular type, it also works on many other types of specimens. This will help to explain its potential capability of improving image quality with similar performance on more 3D data, including those from other OPT imaging systems, which is a part of our current work. In the future we will take further efforts on generalizing the model to other imaging set-ups. In addition, the fluorescent sphere used in the experiments is fixed-size. The effect of sphere size on PSF modelling and deblur performance need to be given more attentions.

3.5 Acknowledgement

The work is partially funded by China Scholarship Council (CSC). We would like to express thanks to Merijn de Bakker (IBL, Leiden, Netherlands), Merel van't Hoff (Leiden University, Netherlands) and Monique Welten (currently: Naturalis Bio Diversity Center, Leiden, the Netherlands) due to their contributions of sample preparation and imaging for the 25 samples used in the experiments.